analytical chemistry

pubs.acs.org/ac Article

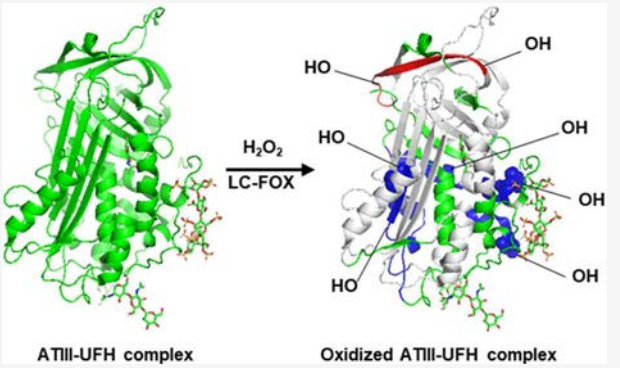
Multidose Inline Size-Exclusion Chromatography–Flash Oxidation for Structural Analysis of Dynamic Protein–Ligand Interactions of Antithrombin III and Unfractionated Heparin

Ajay Sharma, Suman Choudhary, Sandeep K. Misra, Anter A. Shami, Sushil K. Mishra, Zachary C. Drake, Steffen Lindert, and Joshua S. Sharp*

Cite This: *Anal. Chem.* 2026, 98, 6045–6055 Read Online

ACCESS | Metrics & More | Article Recommendations | Supporting Information

ABSTRACT: Hydroxyl radical protein footprinting (HRPF) is a well-established technique used to analyze the binding sites and conformational alterations of proteins. Inline LC-flash oxidation can efficiently capture and characterize structural changes between dynamic protein–ligand complexes as they elute from the LC column. The current work focuses on the development of multidose inline SEC-FOX (size-exclusion chromatography–flash oxidation) for the quantitative topographical analysis of the dynamic protein–ligand complex of human antithrombin III (ATIII) and unfractionated heparin (UFH). ATIII alone and the ATIII-UFH complex were separated by an inline SEC system and flash oxidized at multiple radical doses, followed by proteolytic digestion and LC–MS/MS analysis. A total of 21 oxidized peptides, including three glycopeptides with two major glycoforms each, were reproducibly detected. Six peptides including one glycopeptide (48–53, 58–70, 189–197 A2G2S2 glycoform, 108–114, 333–348, and 360–370) were significantly protected from oxidation upon UFH binding, and one peptide (242–257) showed a significant increase in oxidation upon UFH binding. Residue-level analysis showed that three amino acids (M49, E113, and F329) were significantly protected from modification in the ATIII-UFH complex compared to ATIII alone. Two of these three amino acids are proximal to the known pentasaccharide binding site, while the third is distal and suggests a potential extended interaction of the full-length UFH with ATIII, which was well supported by computational modeling data. We interpret these findings in the context of previously published biophysical data and present a computational model of UFH binding consistent with our findings.



Downloaded via UNIV OF CALIFORNIA LOS ANGELES on July 8, 2026 at 17:51:09 (UTC).
See https://pubs.acs.org/sharingguidelines for options on how to legitimately share published articles.

Higher-order structural (HOS) analysis of proteins under conditions that mimic their natural environment is essential for understanding their biological activity.[1−3] Hydroxyl radical protein footprinting (HRPF) has emerged as a powerful technique for studying the HOS of proteins in their native state.[4−7] In recent years, the introduction of the benchtop Fox Photolysis System has significantly improved the HRPF workflow, making it faster, safer, and more convenient than traditional methods.[7,8] In flash oxidation (FOX), hydroxyl radicals are generated from the photolysis of hydrogen peroxide by using high-energy UV plasma provided by the Fox system. These radicals are highly reactive and short-lived in solution. They rapidly diffuse to the protein surface and covalently modify the solvent-exposed amino acid side chains of the folded proteins. The rate of modification is mainly proportional to the exposure of the side chain to the hydroxyl radical and the inherent chemical reactivity of the amino acid side chain.[6,9] The extent of oxidation at each site is quantified using liquid chromatography-tandem mass spectrometry (LC–MS/MS), providing a structural footprint of the protein's topography.[6−8,10,11] To date, HRPF has been successfully employed in a wide range of systems to identify binding interfaces in protein–protein/protein–ligand interactions, as well as to characterize protein aggregation, oligomerization, structural transitions, and post-translational modifications.[6,10,12−15]

However, probing the HOS of dynamic protein–protein and protein–ligand complexes or mixtures remains challenging due to their size, instability, heterogeneity, and conformational flexibility.[16] Conventional high-resolution structural techniques often face difficulties in resolving conformationally heterogeneous and complex mixtures of proteins or protein–ligand

Received: October 22, 2025
Revised: February 12, 2026
Accepted: February 13, 2026
Published: February 19, 2026



© 2026 The Authors. Published by American Chemical Society

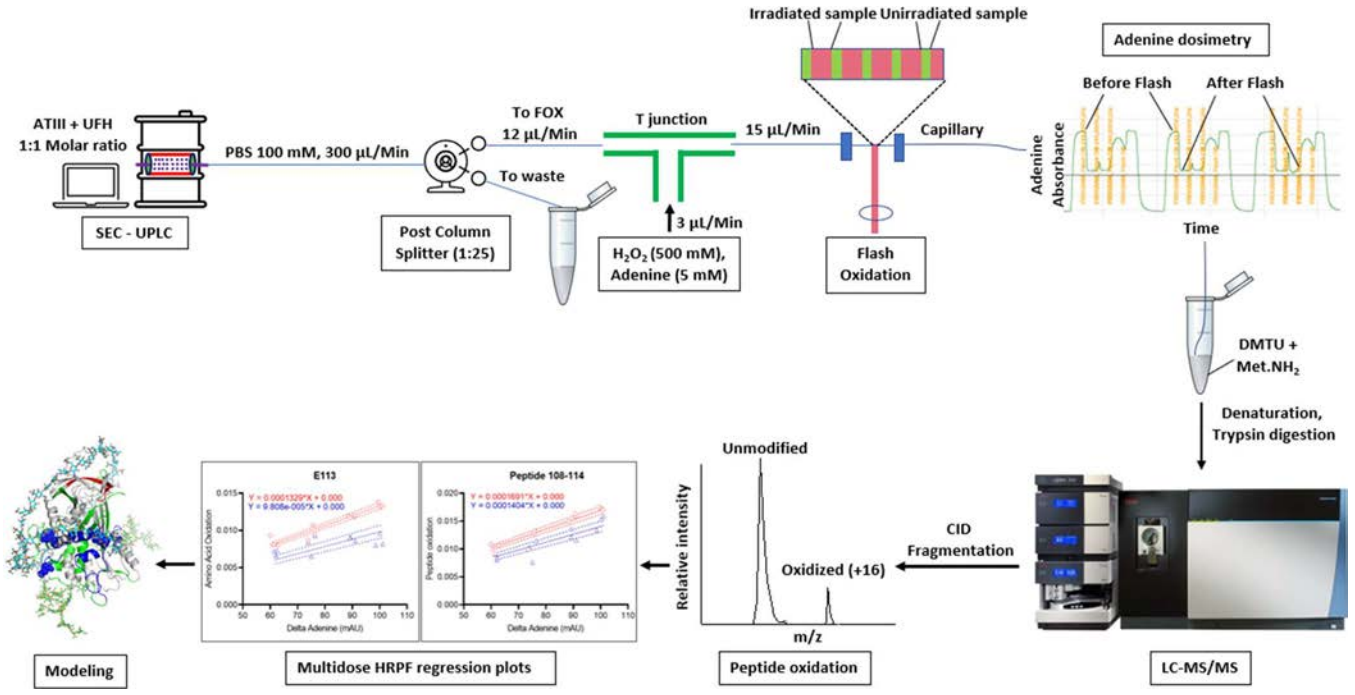


Figure 1. Workflow for inline size exclusion-based LC-FOX. Samples were loaded onto an SEC column, with eluant split postcolumn and flowed through a Fox Photolysis System for footprinting. Each volume of sample was illuminated with a single flash to generate hydroxyl radicals in submillisecond bursts. The modified protein was collected and digested with trypsin. Peptide and amino acid oxidation were quantified by targeted LC−MS/MS analysis, both manually and using FoxWare.

complexes, as the coexistence of multiple conformations can hinder crystallization, reduce signal clarity in crystallography and NMR, and complicate data interpretation.[6,15−17] More recently, inline liquid chromatography−FOX and the closely related LC-fast photochemical oxidation of proteins (LC-FPOP) have been developed as a promising approach to probe the structure of complex and dynamic protein−protein and protein−ligand mixtures in their native solution states, offering new opportunities for detailed, conformer-specific structural characterization of HOS of proteins.[10,18]

Our group has published studies on the development of inline LC-HRPF systems utilizing both isocratic size-exclusion chromatography (SEC) and gradient ion-exchange chromatography. In the first study, an isocratic LC-SEC method was coupled with a traditional excimer laser-based FPOP system. This setup was successfully applied to analyze a synthetic mixture of holomyoglobin and apomyoglobin, as well as the monoclonal antibody adalimumab in both its native and aggregated forms.[10] A subsequent study by Cheng et al.[18] employed inline LC-FOX coupled to weak anion-exchange chromatography using a sodium chloride gradient. This setup enabled real-time analysis of dynamic phosphoproteoform changes in ovalbumin (OVA) during dephosphorylation by alkaline phosphatase. However, these studies were all carried out at single radical doses. Previous work has shown that multidose HRPF data are preferred for use in conjunction with computational modeling.[5,19,20] Multiple doses allow for a more accurate determination of oxidation site reactivity, which in turn makes quantitative determinations based on solvent accessibility more reliable. This level of quantitative rigor is necessary for incorporation into computational modeling, which is a major emerging frontier for HRPF.

The current study presents the development of a multidose semiautomatic inline SEC-FOX platform optimized for the quantitative topographical analysis of dynamic protein−ligand systems. To demonstrate the capabilities of this enhanced system, we applied it to the biologically and clinically relevant ATIII-UFH complex, a model of a dynamic protein−polysaccharide interaction.[21] This represents the first application of multidose LC-FOX. The multidose approach enables a more accurate, reproducible, and robust analysis of conformational changes associated with complex formation, making it more suitable for incorporation into molecular modeling.[5,20] This study also presents the first HRPF analysis of glycopeptides. Protein glycosylation is known to have significant impacts on protein structure and interactions, but previous HRPF work has used deglycosylated strategies to simplify the analysis. Previously published HRPF data on interactions of glycosylated full-length gp120 glycoprotein with b12, coupled with computational modeling, revealed the protection of the gp120 C3 domain due to N330 glycan interaction with the b12 light chain. However, this interaction was inferred based on measurement of peptides that were deglycosylated after HRPF; no measurement of the glycopeptide footprint was made.[12] More recently, Wecksler and coworkers used HRPF of different engineered glycoforms of IgG to measure significant impacts of fucosylation on IgG conformation.[22] Again, this impact was not directly measured at the glycopeptide level but rather inferred based on glycoengineering of the protein prior to HRPF footprinting and deglycosylation. In the current study, we move one step forward toward more direct evaluation of the differential effects of glycan heterogeneity by measurement of HRPF of glycopeptides directly using the ATIII-UFH complex as a model system. While this approach does not allow for global differentiation of the topography of different glycoforms, it does allow for identification of local differences in the

https://doi.org/10.1021/acs.analchem.5c06463
Anal. Chem. 2026, 98, 6045−6055

conformation of the glycopeptide itself based on the glycan structure attached.

MATERIALS AND METHODS

Materials

Calcium chloride ($CaCl_2$), unfractionated heparin (UFH), *N*,*N*′-dimethylthiourea (DMTU), and tris(hydroxymethyl)aminomethane were purchased from Sigma-Aldrich Corp (St. Louis, MO). Dithiothreitol (DTT) was purchased from GoldBio (St. Louis, MO). Hydrogen peroxide (30%), adenine, LC−MS grade formic acid, acetonitrile, methanol, and water were purchased from Fisher Scientific (Fair Lawn, NJ). Methionine amide was purchased from Bachem Americas (Torrance, CA). Human antithrombin III (ATIII) was purchased from Prolytix (Essex Junction, VT). Mono- and dibasic sodium phosphate were purchased from VWR Chemicals (Allentown, PA). Sequencing grade-modified trypsin was purchased from Promega (Madison, WI). Fused silica capillary was purchased from Molex, LLC (Lisle, IL). LC−MS grade trifluoroacetic acid (TFA) was purchased from Thermo Scientific (Waltham, MA).

SEC-MALS Analysis

SEC-MALS (size-exclusion chromatography−multiangle light scattering) analysis was carried out using a Dionex Ultimate 3000 UHPLC system (Thermo Fisher, CA) coupled with a miniDAWN TREOS multiangle light scattering detector (with three angles: 43.6°, 90°, and 136.4°) and an Optilab T-rEX refractometer (Wyatt Technology). Human ATIII and UFH were dissolved (a 1:1 molar ratio) in 100 mM sodium phosphate buffer (pH = 7.4) and incubated for 1 h at 37 °C. The incubated sample was injected onto a size-exclusion column (X Bridge, 250 Å, 2.5 μm, 4.6 × 300 mm, Waters, Milford, MA) using a running buffer of 100 mM sodium phosphate (pH 7.4) at a flow rate of 0.3 mL/min for 10 min in isocratic mode. The UV wavelength was set at 280 nm. All experiments were performed at room temperature (25 °C). SEC-MALS data analysis was performed using ASTRA (7.1.3.25) software (Wyatt Technology).

Inline LC-FOX Instrument Setup

To match the optimum intake flow (15 μL/min) of the Fox Photolysis System[8] (GenNext Technologies), the eluent line (0.3 mL/min) leaving the UV detector of a Dionex Ultimate 3000 UHPLC (Thermo Fisher, CA) system was connected to the inlet of a postcolumn splitter (ASI series 610, split range 5:1 to 100:1) using 250 μm fused silica capillaries. The split ratio was set at 1:25. The low-flow end (12 μL/min) of the postcolumn splitter was connected to a PEEK MicroTee via 250 μm ID fused silica capillary. The high-flow end was diverted to waste by using Teflon tubing with an ID of 500 μm. In the MicroTee, a makeup flow of 3 μL/min containing 500 mM hydrogen peroxide and 5 mM adenine from a Legato 101 syringe pump (KD Scientific, Holliston, MA) equipped with a gastight syringe (Hamilton, Reno, NV) was mixed with the eluant from postcolumn splitter (12 μL/min) at a 1:4 ratio to provide a final concentration of 100 mM hydrogen peroxide and 1 mM adenine. Finally, the eluant (15 μL/min) was passed to the photolysis module of the Fox system (Figure 1).

Inline SEC-FOX

Human ATIII (80 μM) and UFH (80 μM) were dissolved in 100 mM sodium phosphate buffer (pH = 7.4) at a 1:1 molar ratio and incubated for 1 h at 37 °C. Twenty-five μL of the incubated ATIII-UFH mixture was loaded onto a size-exclusion column (ACQUITY UPLC Protein BEH SEC Column, 200 Å, 1.7 μm, 4.6 mm × 150 mm, Waters, Milford, MA). Isocratic separation of UFH-bound and unbound ATIII was performed using 100 mM sodium phosphate, pH 7.4, at a flow rate of 300 μL/min for 10 min. Protein elution was detected at 280 nm. The eluent coming from the UV detector was passed through a postcolumn splitter to a MicroTee, where it was mixed with the adenine and hydrogen peroxide makeup flow coming from an external syringe pump. We used an injection of bovine serum albumin (BSA) as a template protein to measure any changes in peak characteristics and degradation of the SEC separation of BSA dimer and monomer between the UPLC UV detector and the Fox dosimetry detector, which occurs immediately after the UV photolysis cell. We observed peak broadening from ∼30 s to ∼84 s for the dimer and ∼57 s to ∼113 s for the monomer from the UHPLC detector to the FOX dosimeter (Figure S1, Supporting Information). Sample homogeneity was increased by separating the sample flash and collection times. The same conditions were applied to ATII-UFH and ATIII alone peaks during LC-FOX analysis. Each peak was subjected to FOX for 120 s at different lamp voltages (400, 470, 540, and 610 V) and a frequency of 2 Hz. The exclusion volume was 20%, which represents that ∼20% of the solution was unexposed to light, assuming plug flow. This exclusion volume prevents the illumination of the same sample volume multiple times. The oxidized analyte was then passed through the dosimetry module for adenine dosimetry (at 265 nm) to ensure that samples were exposed to equivalent radical doses.[23−27] Control samples without any UV exposure were also run to correct for any background oxidation. Control samples were not exposed to UV flash but were otherwise handled identically. Finally, 25 μL of eluant containing the heart of each peak was collected into 20 μL of quench solution containing 125 mM *N*,*N*′-dimethylthiourea and 43.75 mM methionine amide to react with excess hydrogen peroxide and halt any secondary oxidation, as described in the literature.[28,29] All experiments were performed in triplicate for statistical analysis.

Sample Preparation and LC−MS/MS Analysis

50 mM Tris, pH 8.0, containing 10 mM DTT and 1 mM $CaCl_2$ was added to samples after inline LC-FOX. Samples were incubated for 15 min at 90 °C to denature the protein. Following denaturation, the samples were immediately cooled on ice for 2 min. Again, 10 mM DTT was added, followed by a 1:20 trypsin/protein ratio, to the samples. Samples were incubated at 37 °C for overnight digestion with sample rotation. Finally, digestion was terminated by adding 0.1% formic acid. Digested protein samples were analyzed using an Orbitrap Fusion Tribrid mass spectrometer coupled with a Dionex Ultimate 3000 nanoLC system (Thermo Fisher, CA). The instrument was controlled by Xcalibur version 3.5 (Thermo Fisher, San Jose, CA). Before LC−MS/MS analysis, a final concentration of 10 mM DTT was added to each digested sample, followed by incubation at 65 °C for 20 min. The incubated samples were loaded onto an Acclaim C18 (5 μm, 0.3 × 5 mm) trap column and eluted onto an Acclaim PepMap C18 nanocolumn (0.75 mm × 150 mm, 2 μm, Thermo Fisher Scientific). Peptide separation was performed using 0.1% formic acid in water (solvent A) and 0.1% formic acid in acetonitrile (solvent B) at a flow rate of 0.3 μL/min using gradients of 2% solvent B for 2 min, 7% B for 1 min, then to 32% B for 39 min, ramped to 95% B for 1 min, held for 2 min, and then returned to 2% B for 2 min and held for 8 min. Peptides were eluted directly into the nanospray source of the Orbitrap Fusion instrument using a conductive nanospray emitter. The nESI source was operated in the positive ion mode. The spray voltage and temperature of the ion transfer tube were set to 2300 V and 300 °C, respectively. An Orbitrap nominal resolution of 60,000 and an RF lens setting of 60 were used. Peptide fragmentation was done by CID with an isolation window of 2 m/z units. Full MS scans were acquired from m/z 250 to 2000, followed by subsequent MS2 scans of the top 10 most abundant peptide ions.

LC-FOX Data Analysis

After tryptic digest, one sample of the ATIII-UFH complex was subjected to untargeted analysis using LC−MS/MS. The data obtained were analyzed by Byonic (v4.4.2, Protein Metrics, San Carlos, CA) to determine protein sequence coverage, with a mass error of 10 ppm at the precursor level and 0.4 Da for the fragments. The Byonic search parameters included all possible major oxidation modifications as variable modifications,[30] but only net additions of oxygen were observed. The sequence coverage of the sample was greater than 80%. The file was run on FoxWare (v2.1.2, GenNext Technologies, CA) to get a mass inclusion list of peptides, which was used to generate the targeted method on an Orbitrap Fusion Tribrid mass spectrometer coupled with a Dionex Ultimate 3000 nanoLC system (Thermo Fisher, CA). The mass inclusion list of peptides used for targeted method development is presented in Table S1,

https://doi.org/10.1021/acs.analchem.5c06463
Anal. Chem. 2026, 98, 6045−6055

Table 1. Peptide-Level Multidose HRPF Results[a]

	ATIII alone			ATIII-UFH complex			
Peptide	Slope of ATIII ± Std. Error	95% Confidence Intervals	R^2	Slope of ATIII-UFH ± Std. Error	95% Confidence Intervals	R^2	Slope of ATIII-UFH/ATIII only
1-13	0.002379± 0.000119	0.002117 to 0.002641	0.9732	0.001932± 0.0001372	0.001630 to 0.002234	0.9443	0.8121
14-24	0.006688± 0.0005289	0.005524 to 0.007852	0.9356	0.007362± 0.0004394	0.006395 to 0.008329	0.9623	1.1008
30-46	0.0006958± 0.0000183	0.0006555 to 0.0007361	0.9924	0.0006732± 0.00001846	0.0006325 to 0.0007138	0.9918	0.9675
48-53	**0.00487± 0.0002838**	**0.004245 to 0.005494**	**0.964**	**0.002173± 0.0001361**	**0.001873 to 0.002472**	**0.9587**	**0.4462**
58-70	**0.0004179± 0.00001663**	**0.0003813 to 0.0004545**	**0.9829**	**0.0003162± 0.00001583**	**0.0002814 to 0.0003510**	**0.9732**	**0.7566**
71-91	0.006913± 0.0004394	0.00546 to 0.007880	0.9575	0.005902± 0.000335	0.005164 to 0.006639	0.9658	0.8537
92-107 A2G2S2 Glycoform	0.008510± 0.0004461	0.007528 to 0.009492	0.9707	0.007075± 0.0003379	0.006331 to 0.007819	0.9755	0.8314
92-107 A2G2S1 Glycoform	0.008876± 0.0004816	0.007816 to 0.009936	0.9686	0.007445± 0.0002389	0.006919 to 0.007970	0.9888	0.8422
108-114	**0.0001691± 0.000003377**	**0.0001616 to 0.0001765**	**0.9956**	**0.0001404± 0.000004382**	**0.0001308 to 0.0001500**	**0.9894**	**0.8303**
115-125	0.0002336± 0.00003178	0.0001637 to 0.0003036	0.8308	0.0003397± 0.0000219	0.0002915 to 0.0003879	0.9563	1.4542
151-169 A2G2S2 Glycoform	0.0009980± 4.490e-005	0.0008992 to 0.001097	0.9782	0.001073± 5.163e-005	0.0009593 to 0.001187	0.9752	1.0752
151-169 A2G2S1 Glycoform	*0.0001877± 4.324e-005*	*9.250e-005 to 0.0002828*	*0.6313*	0.0008002± 7.510e-005	0.0006349 to 0.0009655	0.9117	*4.2632*
170-176	0.000294± 0.00000957	0.0002729 to 0.0003150	0.9885	0.000275± 0.00001871	0.0002338 to 0.0003162	0.9515	0.9354
189-197 A2G2S2 Glycoform	**0.001316± 5.523e-005**	**0.001194 to 0.001437**	**0.981**	**0.0007838± 6.913e-005**	**0.0006317 to 0.0009360**	**0.9212**	**0.5956**
189-197 A2G2S1 Glycoform	0.001310± 0.0001223	0.001041 to 0.001579	0.9125	*0.0006845± 0.0001522*	*0.0003496 to 0.001019*	*0.6478*	*0.5225*
229-235	0.0002035± 0.000005347	0.0001917 to 0.0002153	0.9925	0.0002091± 0.000004555	0.0001990 to 0.0002191	0.9948	1.0275
242-257	**0.003191± 0.0001183**	**0.002931 to 0.003451**	**0.9851**	**0.004018± 0.00007623**	**0.003850 to 0.004186**	**0.9961**	**1.2592**
263-275	0.0004354± 2.09E-05	0.0003895 to 0.0004813	0.9754	0.0004224± 0.00001301	0.0003937 to 0.0004510	0.9897	0.9701
325-332	0.0003852± 1.02E-05	0.0003628 to 0.0004076	0.9924	0.0003384± 0.00001188	0.0003122 to 0.0003645	0.9866	0.8785
333-348	**0.006741± 0.0001297**	**0.006456 to 0.007027**	**0.9959**	**0.005938± 0.0001254**	**0.005599 to 0.006277**	**0.9927**	**0.8809**
351-359	0.000363± 0.000009498	0.0003421 to 0.0003839	0.9925	0.0003189± 0.00001497	0.0002860 to 0.0003519	0.9764	0.8785
360-370	**0.000754± 0.00001968**	**0.0007107 to 0.0007973**	**0.9926**	**0.0006518± 0.00002207**	**0.0006032 to 0.0007004**	**0.9875**	**0.8645**
414-425	0.004605± 0.0001453	0.004286 to 0.004925	0.9892	0.004963± 0.0001168	0.004706 to 0.005220	0.9939	1.0777
426-432	0.0008173± 0.00003557	0.0007390 to 0.0008956	0.9796	0.001019± 0.00008384	0.0008349 to 0.001204	0.9307	1.2468

[a]Blue: significantly protected, red: significantly exposed. A peptide was considered significantly changed (protected or exposed) if the 95% confidence intervals for its oxidation extent in the ATIII-UFH complex and ATIII alone did not overlap. Italics: peptide not included in analyses due to low R^2 values of regression.

Supporting Information. Finally, a targeted method was used for the analysis of all of the samples obtained from tryptic digests of the ATIII-UFH complex and ATIII alone. Targeted analysis focuses on predefined peptides, which is necessary for residue-level analysis in order to capture all oxidation isomers that might be lost in an untargeted approach due to dynamic exclusion and/or low signal intensity. The LC−MS/MS data obtained after targeted analysis of the ATIII-UFH complex and ATIII alone were again analyzed by using Byonic to determine protein sequence coverage. The mass spectrometry proteomics data have been deposited to the ProteomeXchange Consortium via the PRIDE[31] partner repository, and the data are available via ProteomeXchange with identifier PXD034906.

The level of oxidation in each peptide and amino acid was determined using FoxWare, with manual auditing and adjustment where necessary. The intensities of each unoxidized peptide and their corresponding oxidation products observed in the selected ion chromatogram (mass tolerance: 10 ppm and smoothing: 3 points) were used to manually calculate the average oxidation events per peptide/amino acid in the sample using Xcalibur (Thermo Fisher, San Jose, CA), as previously reported.[5,32,33] Briefly, peptide-level oxidation was calculated by adding the ion intensities of all the oxidized peptides multiplied by the number of oxidation events required for

https://doi.org/10.1021/acs.analchem.5c06463
Anal. Chem. 2026, 98, 6045−6055

Table 2. R^2, Slope, and 95% Confidence Intervals Correspond to ATIII Alone and ATIII-UFH Complex for Amino Acid-Level Multidose Oxidation Data[a]

	ATIII alone			ATIII-UFH complex			
Amino Acid	Slope of ATIII ± Std. Error	95% Confidence Intervals	R^2	Slope of ATIII-UFH ± Std. Error	95% Confidence Intervals	R^2	Slope of ATIII-UFH/ATIII only
P4	0.00007618± 0.000002641	7.037e-005 to 8.199e-005	0.987	0.00007279± 0.000003022	6.614e-005 to 7.944e-005	0.9811	0.9555
W49	**0.002164± 0.0001001**	**0.001943 to 0.002384**	**0.977**	**0.00148± 0.0001051**	**0.001249 to 0.001712**	**0.9811**	**0.6839**
M89	0.007517± 0.0004797	0.006461 to 0.008573	0.9571	0.006503± 0.0003438	0.005747 to 0.007260	0.9702	0.8651
E113	**0.0001329± 0.000002181**	**0.0001281 to 0.0001377**	**0.997**	**0.00009808± 0.000003983**	**8.931e-005 to 0.0001068**	**0.9822**	**0.7380**
F175	0.00006164± 0.000008967	4.191e-005 to 8.138e-005	0.8137	*0.00003215± 0.000007231*	*1.624e-005 to 4.807e-005*	*0.6462*	*0.5216*
M251	0.001067± 0.00006978	0.0009133 to 0.001220	0.955	0.001287± 0.00007397	0.001124 to 0.001450	0.9649	1.2062
M252	0.001431± 0.00008633	0.001241 to 0.001621	0.9615	0.001713± 0.00008594	0.001524 to 0.001903	0.9731	1.1971
Y253	0.0002998± 0.00004202	0.0002073 to 0.0003923	0.8223	0.0004281± 0.00002618	0.0003704 to 0.0004857	0.9605	1.4279
F329	**0.0002049± 0.000009151**	**0.0001848 to 0.0002251**	**0.9785**	**0.0001413± 0.000007056**	**0.0001257 to 0.0001568**	**0.9733**	**0.6896**
M338	0.005608± 0.0001159	0.005353 to 0.005863	0.9953	0.005566± 0.00008011	0.005390 to 0.005743	0.9977	0.9925
V341	*0.0001299± 0.00002708*	*7.028e-005 to 0.0001895*	*0.6776*	0.0001117± 0.0000143	8.027e-005 to 0.0001432	0.848	*0.8599*
P346	0.0002226± 0.00001714	0.0001849 to 0.0002603	0.9388	0.0002034± 0.00001528	0.0001697 to 0.0002370	0.9416	0.9137
Y363	0.0004376± 0.00002936	0.0003730 to 0.0005022	0.9528	0.0003775± 0.0000129	0.0003491 to 0.0004059	0.9873	0.8627
A367	0.0001574± 0.000005482	0.0001454 to 0.0001695	0.9868	0.0001391± 0.000005409	0.0001272 to 0.0001510	0.9835	0.8837
M423	0.004328± 0.0001432	0.004013 to 0.004643	0.9881	0.004808± 0.0001135	0.004558 to 0.005057	0.9939	1.1109
K432	0.0003443± 0.000007295	0.0003282 to 0.0003603	0.9951	0.0003466± 0.00001205	0.0003200 to 0.0003731	0.9869	1.0067

[a]Blue: significantly protected; an amino acid was considered significantly changed (protected or exposed) if the 95% confidence intervals for its oxidation extent in the ATIII-UFH complex and ATIII alone did not overlap. Italics: residue not included in analyses due to low R^2 values of regression.

the mass shift (e.g., one event for +16, two events for +32) and then divided by the sum of the ion intensities of all unoxidized and oxidized peptide masses, as represented by the following equation:[7]

$$P = [(I(+16)\text{oxidized} \times 1 + (\text{I} + 32)\text{oxidized} \times 2 + (\text{I} + 48)\text{oxidized} \times 3 + \ldots)/I\text{unoxidized} + I(+16)\text{oxidized} + I(+32)\text{oxidized} + I(+48)\text{oxidized} + \ldots)]$$

P represents the average oxidation events per peptide, and I is the area under the curve for peaks of oxidized and unoxidized peptides. All major identified oxidation products are the net addition of one or more oxygen atoms.

The level of oxidation in different glycosylated peptides (N-linked glycans of type A2G2S2 and A2G2S1) was calculated separately manually in the same way as that explained above using Xcalibur. Among the two glycoforms, A2G2S2 is the major one with ∼85% relative abundance, while A2G2S1 is the minor one with ∼15% relative abundance.[34] For glycosylated peptides, the level of oxidation was calculated for one oxidation event (+16) only, and the peaks used for these calculations were M+1 isotopologue peaks due to their increased intensity and decreased overlap with other products in the spectrum.

Mean oxidation levels from the triplicate control samples with no flash, at both the peptide and residue levels, were subtracted from the multidose data collected at different voltages to obtain normalized values, where the oxidation at 0 V equals 0. The three 0-V samples served as negative controls (Tables S2 and S3, Supporting Information). The average oxidation values at both the peptide and amino acid levels from these controls were subtracted from all other samples to normalize the data and eliminate background oxidation, which resulted in an accurate assessment of protein structural changes or interactions.

Statistical Analysis

Linear regressions with 95% confidence intervals were plotted for each peptide, glycoform, and individual residue using GraphPad Prism (version 9.0.0), with the Y-intercept set to zero, representing no oxidation above background in the absence of flash. Regressions were considered high quality if the R^2 value, generated from linear regression plots when the Y-intercept is constrained to zero, was >0.8 (Tables 1 and 2). Only ATIII alone peptide 151−169 A2G2S1 glycoform (R^2 − 0.63), ATIII-UFH complex peptide 189−197 A2G2S1 glycoform (R^2 − 0.65), ATIII-UFH complex amino acid F175 (R^2 − 0.65), and ATIII alone amino acid V341 (R^2 − 0.68) had R^2 < 0.8; these regressions were not considered for evaluating significant protection and exposure upon UFH binding, nor for evaluating the differential impact of glycoforms on conformation or UFH binding. We consider changes to be significant if their 95% confidence interval values did not overlap.

Computational Modeling of the ATIII-UFH Complex

Active-state structures of human ATIII were generated using AlphaFold3 (AF3).[35] 3500 structures were generated using random integer seeds to increase model variability and obtain a structure consistent with protection of the 329−340 region. N-linked glycans of type A2G2S2 were modeled at four known glycosylation sites (N96, N135, N155, and N192) using ligands from the chemical component dictionary codes for each monosaccharide, followed by indication of glycan bonds through manual entries of bond pairs represented as

https://doi.org/10.1021/acs.analchem.5c06463
Anal. Chem. 2026, 98, 6045−6055

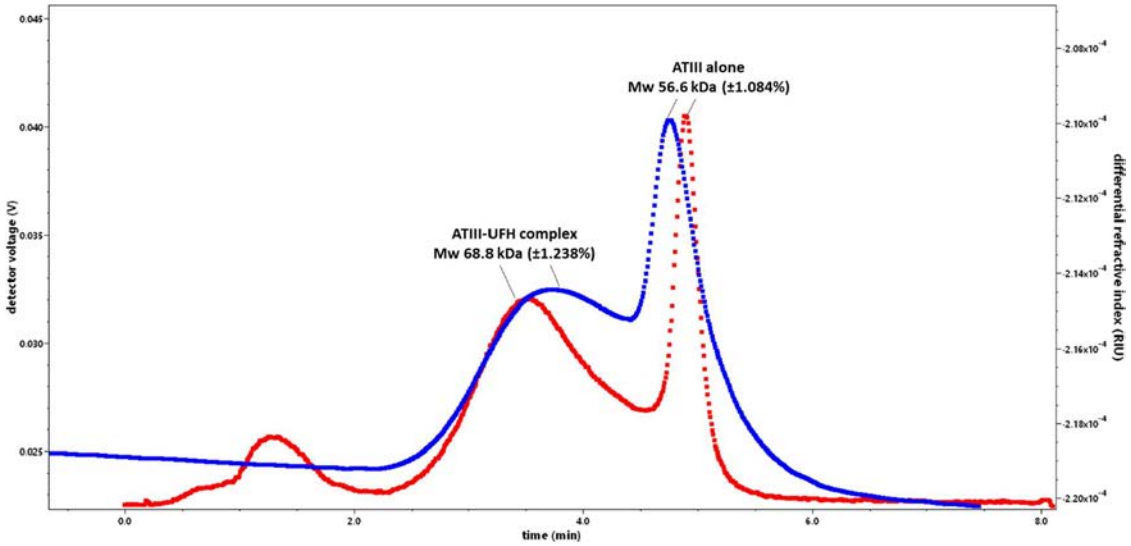


Figure 2. SEC-MALS of ATIII alone and the ATIII-UFH complex. (Blue) refractive index and (red) multiple angle light scattering detector results. Each peak is labeled with the calculated molecular weight.

'bondedAtomPairs' in the input JSON file. A 52-unit UFH polysaccharide ligand was constructed from a single SMILES string representation. Several AF3 structures were identified with UFH bound. A molecular mechanics minimization, followed by a short molecular dynamics simulation, was performed to test the stability of the modeled ATIII-UFH complex. The AF3 structures of ATIII-UFH with glycosylation were prepared using the CHARMM-GUI Glycan Modeler.[36,37] Input files were generated with the CHARMM36m[37] force field applied to the protein and CHARMM36[38] applied to all other components. Systems were explicitly solvated with TIP3P water within 10Å and neutralized with K^+/Cl^- ions at 0.15 M concentration.[39] After 10,000 steps of minimization, equilibration was conducted using an NVT ensemble at 303.15 K using a Langevin thermostat. Production simulations were run in the NPT ensemble at 303.15 K and 1 atm using the Langevin piston barostat. All simulations were run using a 2 fs time step with SHAKE applied to hydrogen-containing bonds.[40] A 12 Å cutoff was used for van der Waals interactions, and long-range electrostatics were treated with Particle Mesh Ewald (sixth-order interpolation; grid spacing of 1 Å). Nonbonded interactions used a 10−12 Å switching scheme and a 16 Å pairlist. Trajectories were saved every 5 ps. Prepared systems were subjected to 0.25 ns equilibration and a 5 ns production NAMD[38,42] simulation, which was performed using default CHARMM-GUI parameters. All 3D protein images were generated using PyMOL (Version 3.1.3.1).[41]

RESULTS

SEC-MALS Analysis of Unbound ATIII and ATIII-UFH Complex

Molecular weight determination of UFH-bound and unbound ATIII was carried out using SEC-MALS. The SEC-UV curve showed two distinct peaks at a 0.3 mL/min flow rate; the first peak corresponded to the ATIII-UFH complex, and the second peak corresponded to ATIII alone. The SEC-MALS results revealed that the calculated molar mass of the ATIII-UFH complex was 68.8 kDa (±1.238%) with a polydispersity of 1.005×10^4 (±1.755%), and the molar mass of the ATIII alone was 56.6 kDa (±1.084%) with a polydispersity of 1.001×10^4 (±1.529%) (Figure 2). The current results are consistent with the ATIII-UFH binary complex, in agreement with already published data on the formation of ATIII and the heparin/UFH complex.[43]

Inline LC-FOX of Equimolar Mixture of ATIII and UFH

ATIII alone reproducibly elutes by isocratic SEC at ∼4.47 min, whereas the ATIII-UFH complex elutes at ∼3.96 min. At this molar ratio, roughly half of ATIII forms a complex with UFH, and the other half remains free. This dynamic mixture was subjected to inline LC-FOX as each conformer eluted from the column, as outlined in Figure 1. All labeled samples were collected as guided by the UV trace of UPLC, from 3.2 to 4.15 min and 4.4 to 5.35 min (Figure S2, Supporting Information). Adenine dosimetry shows that all replicates for the ATIII-UFH complex and ATIII alone at a particular voltage have comparable effective radical doses (Figure S3, Supporting Information).

The current result revealed that we were able to perform the glycoform-resolved structural analysis of glycan intact protein followed by the HRPF experiment and tryptic digestion. Linear regressions of multidose data are shown for all peptides, including both major glycoforms of the three observed glycopeptides, for both ATIII alone and the ATIII-UFH complex (Figure S4, Supporting Information). For non-glycopeptides, residue-level regressions were also generated where it was possible to identify specific site(s) of oxidation (Figure S5, Supporting Information). The results of oxidation analysis for the peptide level and residue level are presented in Tables 1 and 2. Oxidation differences in the respective peptides and amino acids were compared for bound (ATIII-UFH complex) and unbound (ATIII alone) conformers of ATIII.

With one exception, all of the replicates showed sequence coverage >80% (Table S4, Supporting Information). A total of 21 common peptides including three glycopeptides with two glycoforms A2G2S2 and A2G2S1 were reported across all doses (different voltages) by LC−MS/MS analysis. From these peptides, residue-level oxidation could be measured for 16 different amino acids, representing a strong depth of footprinting coverage for the ATIII protein (Figure S6, Supporting Information).

Out of 21 oxidized peptides, six showed a significant decrease in oxidation level (peptides 48−53, 58−70, 108−114, 189−197 A2G2S2 glycoform, 333−348, and 360−370), indicating their protection from solvent upon UFH binding.

https://doi.org/10.1021/acs.analchem.5c06463
Anal. Chem. 2026, 98, 6045−6055

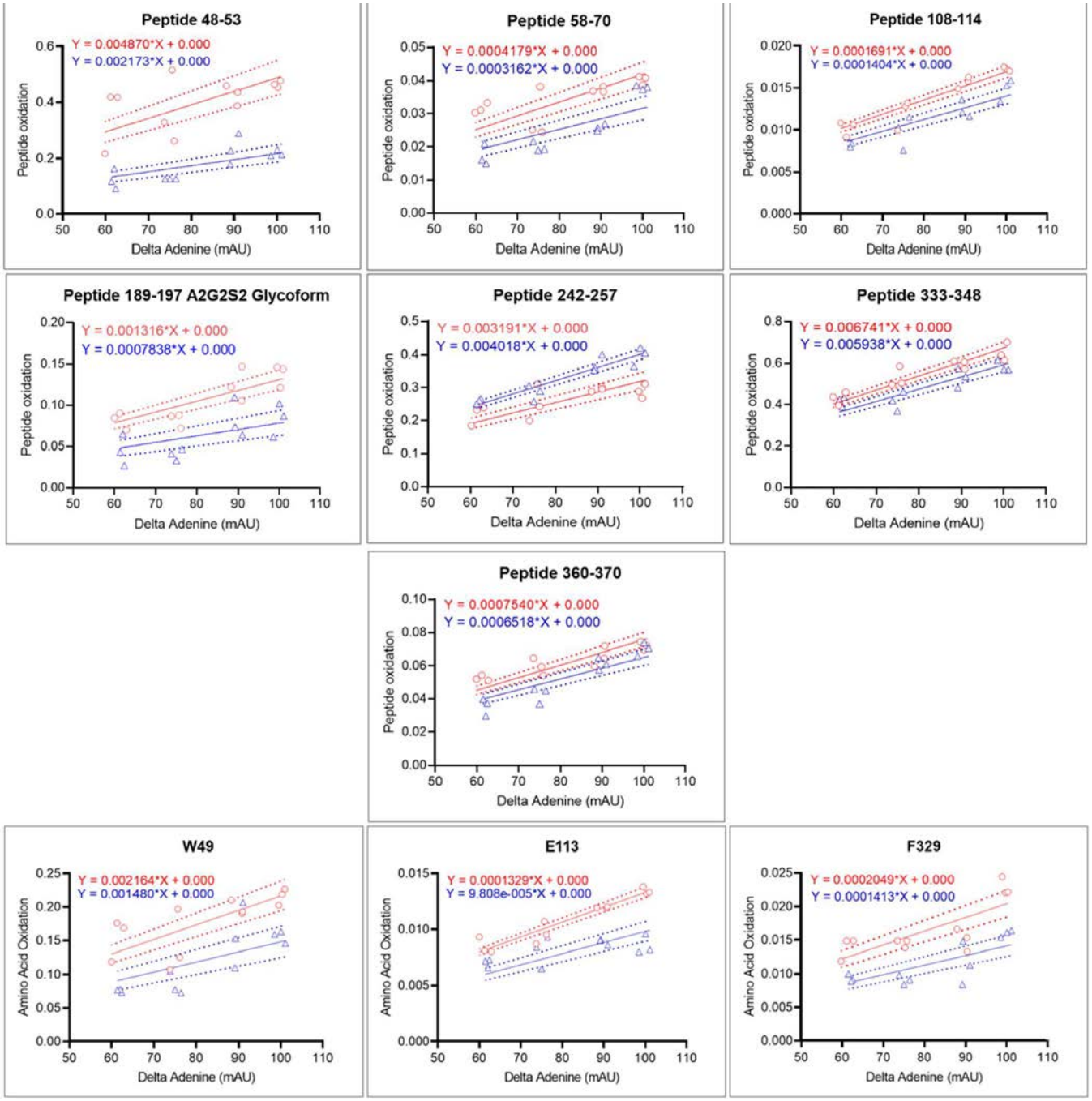


Figure 3. HRPF regression plots for significantly protected and exposed peptides and amino acids. Oxidation of ATIII alone is presented in red, and the ATIII-UFH complex is presented in blue after multidose HRPF.

Only one peptide (peptides 242−257) showed a significant increase in oxidation level upon UFH binding, indicating its exposure to solvent in the ATIII-UFH complex compared to ATII alone (Table 1). Similarly, a total of 16 common oxidized amino acids were quantified among all of the radical doses by LC−MS/MS analysis. Three amino acids showed a significant decrease in oxidation level, indicating their protection from solvent in the ATIII-UFH complex compared to ATII alone (W49, E113, and F329), whereas none of the amino acids showed a significant increase in oxidation level in the ATIII-UFH complex compared to ATII alone (Table 2).

Out of all six significantly protected peptides, we were able to identify statistically significant residue-level protection in two of them (W49 in peptides 48−53; E113 in peptides 108−114), as presented in Figure 3. Furthermore, the significantly protected peptides 48−53, 58−70, and 108−114, identified in the current study, are located around or near the known pentasaccharide and heparin binding site of ATIII.[44,45] None of the quantified residue-level labeling in four significantly protected (58−70, 189−197 A2G2S2 glycoform, 333−348, and 360−370) and one significantly exposed (242−257) peptides reached statistical significance. This could be due to low modification efficiency at specific residues, which limits the confident assignment of oxidation at a specific amino acid and lack of sufficient CID fragment ions to differentiate oxidation among different amino acids, both of which negatively impact

https://doi.org/10.1021/acs.analchem.5c06463
Anal. Chem. 2026, 98, 6045−6055

the ability to assign the oxidized peptide signal to an individual amino acid with confidence. Additionally, the distribution of oxidation signals across multiple residues within the peptide dilutes the effect of modification at any single amino acid and can reduce the statistical power of the analysis at the residue level. Furthermore, amino acid F329 showed significant protection, whereas protection of the corresponding peptides 325−332 did not quite reach statistical significance. This can occur when protection at one residue is offset by increased oxidation or high variability at others within the same peptide, masking the net change at the peptide level. Interestingly, residue R47 near peptide 48−53 and residues E113 and K114 of peptide 108−114 have been reported to be involved directly in ATIII binding to fondaparinux, a synthetic heparin pentasaccharide, and to heparin.[44−48] Previous studies revealed that three basic residues K114, K125, and R129 of ATIII were the key hotspots for binding to the ATIII-specific pentasaccharide. Among these, K114 has been known to be the most critical, as its substitution leads to a 10^5-fold reduction in heparin affinity, compared to a 150−600-fold loss for K125, a 400−2500-fold loss for R129, and a 20−30-fold loss for R47. Additionally, K114 has been reported to enhance the forward rate constant of the second step in ATIII-heparin binding. These findings highlight the pivotal role of K114 in facilitating ATIII-heparin binding,[45,49] which corresponds well to our findings for peptides and amino acids surrounding the pentasaccharide binding region.

Out of four glycopeptides, three (92−107, 151−169, and 189−197) were reported across all doses (different voltages) by LC−MS/MS analysis for both A2G2S2 and A2G2S1 glycoforms. However, the less abundant A2G2S1 glycoform gave poor regression-quality results for one glycopeptide in ATIII alone (151−169) and for one glycopeptide in the ATIII-UFH complex (189−197), making comparisons of the impact of the glycoform for these two peptides challenging. When measuring the impact of glycoform on the conformation of ATIII alone, the two peptides for which we have high-quality data for both glycoforms (92−107 and 189−197) show no impact of glycoform on the peptide footprint (Table 1). Similarly, when measuring the impact of glycoform on the conformation of the ATIII-UFH complex, the two glycopeptides for which we have high-quality data for both glycoforms (92−107 and 151−169) show no impact of glycoform on the peptide footprint (Table 1). We can examine the impact of glycoform on the change in footprint upon UFH binding for only one peptide (92−107). The A2G2S2 major glycoform shows modest protection upon UFH binding, with the ratio of the regression slope of the ATIII:UFH complex to the regression slope of ATIII alone being 0.8314. For the minor A2G2S1 glycoform, this slope is an almost-identical 0.8422. Taken together, these data indicate that glycoform has no substantial impact on the conformation of ATIII or the UFH-ATIII complex. To the best of our knowledge, this is the first report using glycoform-specific multidose HRPF to probe the impact of glycoforms on local topography and ligand binding.

In Silico Modeling of ATIII with UFH

We employed deep-learning methods for modeling heparin with ATIII. Specifically, we generated 3500 AlphaFold3 structures of ATIII with heparin and N-linked A2G2S2 glycans at residues N96, N135, N155, and N192. We identified several AF3 complexes where the heparin was positioned close to the region of peptide 329−340. To probe structural stability, the AF3 structure was subsequently minimized, and a short MD simulation was performed. We observed that heparin maintained close proximity to the 329−340 peptide, with a minimum distance of 3.8Å.

DISCUSSION

The computational model of the ATIII-UFH complex provides a plausible vehicle for interpretation of the HRPF data when plotted on the model (Figures 4 and 5A). The results indicate

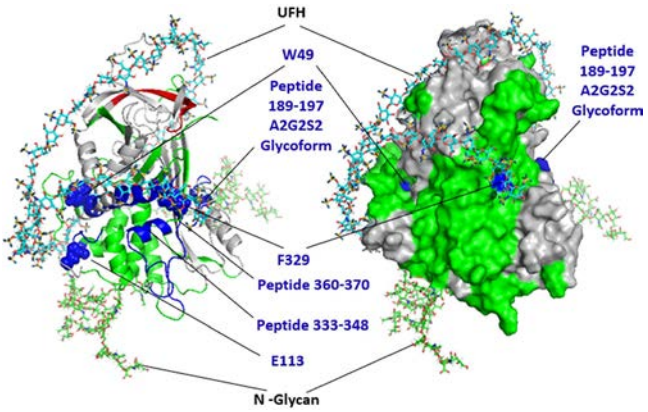


Figure 4. Active form of ATIII wrapped around by UFH (left: ribbon model; right: space-filling model), showing protection of F329 and peptides 189−197 A2G2S2 glycoform, 333−348, and 360−370 by wrapping of UFH around ATIII. Blue regions are areas showing protection, red areas represent exposure, green represents areas where no statistically significant change in oxidation is measured, and gray regions have no consistent oxidized peptide observed in all replicates when plotted using multidose inline LC-HRPF analysis data upon binding with UFH.

that the region of ATIII (peptides 48−53, 58−70, 108−114; amino acids W49, E113) near the consensus high-affinity pentasaccharide site experiences significant protection from oxidation upon binding to UFH.

The protection at peptides 189−197 A2G2S2 glycoform, 333−348, 360−370, and F329 amino acid, distal to the minimal specific pentasaccharide binding site, can be explained on the basis of the 3D structure of ATIII and the ATIII-UFH complex obtained after in silico modeling (Figure 4). The 3D structure of ATIII-UFH clearly showed that peptides 189−197 A2G2S2 glycoform, 360−370, and F329 are protected by UFH binding. The wrapping of UFH around ATIII in the ATIII-UFH complex covered the area around peptides 189−197 A2G2S2 glycoform, 360−370, and F329, which resulted in reduction of solvent/hydroxy radical accessibility to these peptides/amino acids and hence protect them from oxidation compared to ATIII alone. Molecular dynamics simulation revealed that heparin maintained close proximity to the 329−340 peptide, with a minimum distance of 3.8Å, which supports the interpretation of this protection being due to local binding of the longer UFH chain, distal to the pentasaccharide binding site.

The significant protection of peptides 108−114 and 333−348 and amino acids E113 and F329 in the ATIII-UFH complex compared to ATIII alone in the present study was also supported by the study conducted by Listigovers et al.[50] Listigovers et al. studied allosteric changes in ATIII upon binding to fondaparinux and natural heparins (dp20) using time-resolved electrospray ionization−millisecond hydrogen-

https://doi.org/10.1021/acs.analchem.5c06463
Anal. Chem. 2026, 98, 6045−6055

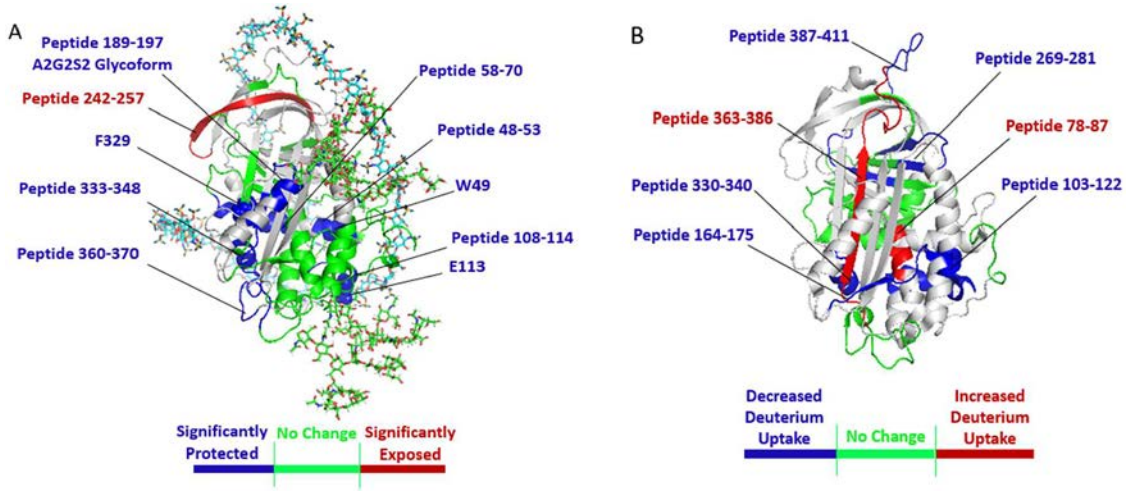


Figure 5. Comparison of HRPF and HDX data. (A) HRPF data mapped onto the structure of ATIII. The active form of ATIII shows protected (blue) and exposed (red) regions when plotted using multidose inline LC-HRPF analysis data upon binding with UFH. Green regions are areas where no statistically significant change in oxidation is measured; and gray regions indicate no consistent oxidized peptide observed in all replicates. Peptide-level data are mapped in the ribbon diagram, while residue-level data are shown as spherical models. (B) Uptake of HDX mapped to the dp20 bound state of ATIII (PDB 1E03),[51] as reported by Listigovers et al.[50] Red: increased %D; blue: decreased %D; green: no significant change; gray: no sequence coverage.

deuterium exchange mass spectrometry and evaluated these conformational changes for complex stability in the gas phase. Peptides 103−121, 103−122, 106−122, 109−122, 109−123, 164−175, 269−281, 330−340, 387−402, 388−402, 388−411, and 390−402 showed a decrease in % D uptake, whereas peptides 78−87, 363−387, and 365−373 indicated an increase in % D uptake in the ATIII-dp20 complex compared to ATIII alone (Figure 5B).[50]

In addition, the published data revealed that widespread topographical changes are induced in ATIII upon binding with UFH, and these changes are not limited to binding sites.[50] Thus, the significant exposure of peptide 242−257 may be attributed to allosteric conformational changes induced in ATIII upon binding with UFH. However, it must be remembered that HDX data and HRPF data probe fundamentally different biophysical parameters, with HDX data being dominated by protein backbone conformation and dynamics, while HRPF data report on side-chain topography. These data may be correlated, but they should not be expected to be identical; they are best viewed as complementary data.

CONCLUSIONS

The present results serve as strong validation of multidose SEC-FOX HRPF as a valuable method for protein conformational analysis for systems where conformers can be separated. Our method is able to examine the heterogeneous and dynamic complex of UFH with ATIII and detect protection not only at the known pentasaccharide binding site but also at distal sites that are supported by HDX results as well as by in silico modeling. We also present HRPF measurements of individual glycoforms by direct footprinting measurements of glycopeptides; to our knowledge, this is the first time that such footprinting of glycopeptides has been reported. While HRPF of glycopeptides is limited to revealing the local impact of glycosylation on topography (as we cannot link a particular glycopeptide to other measured peptides), it does provide the first evidence that such measurements are possible. Furthermore, in contrast to previous inline LC-HRPF studies,[10,18] which were conducted at single doses of hydroxyl radicals and required manual flow adjustments or compromised flow rates, the current study introduces a semiautomated inline LC-FOX workflow evaluated at multidose analysis for higher robustness and accuracy. When performing LC-FOX, it is important to set up the experiment to minimize coelution of the conformers to be measured and to alter the flash and sample collection times to minimize the analysis of coeluted conformers. Work is underway with a focus on extending this platform to more complex and biologically relevant dynamic systems, particularly those that are difficult to purify or isolate in distinct conformational states. In such cases, inline LC-FOX holds promise for resolving subtle structural differences that are otherwise inaccessible by using conventional methods.

ASSOCIATED CONTENT

Supporting Information

The Supporting Information is available free of charge at https://pubs.acs.org/doi/10.1021/acs.analchem.5c06463.

Figure S1: (A) UPLC chromatogram of BSA dimer (Peak 1) and monomer (Peak 2), (B) chromatogram of BSA taken from the Fox dosimetry detector immediately postflash cell shaded areas represent the sample volume that was flashed (red) and collected (blue), to minimize colabeling of the two peaks, no sample was collected for 30 s between the blue-labeled regions; Figure S2: UPLC chromatogram of all replicates used for the multidose inline LC-HRPF, shaded areas represent the sample volume that was collected for (red) ATIII alone and (blue) ATIII-UFH complex, to minimize colabeling of the two conformers, no sample was collected for 30 s between the labeled regions; Figure S3: bar graph of the adenine absorbance for multidose inline LC-HRPF for each replicate of ATIII alone (blue) and ATIII-UFH complex (red); Figure S4: HRPF regressions for peptides level oxidation − ATIII alone (red) and ATIII-UFH complex (blue) after multidose HRPF with their 95% confidence interval values; Figure S5: HRPF regressions for amino acids level oxidation -

https://doi.org/10.1021/acs.analchem.5c06463
Anal. Chem. 2026, 98, 6045−6055

ATIII alone (red) and ATIII-UFH complex (blue) after multidose HRPF with their 95% confidence interval values; Figure S6: depth of HRPF probe of ATIII-UFH, peptides that are measured as oxidized in all replicates at all four voltages tested are highlighted in yellow, amino acids where oxidation was quantified at residue level are underlined, regions where oxidation was not measured in all replicates are italicized; Table S1: targeted mass list of peptides of ATIII-UFH complex for the residue-level analysis using LC−MS/MS on Orbitrap Fusion; Table S2: peptide-level oxidation in different replicates at 0 V; Table S3: residue-level oxidation in different replicates at 0 V; and Table S4: percentage sequence coverage of each replicate of ATIII alone and ATIII-UFH complex (PDF)

AUTHOR INFORMATION

Corresponding Author

Joshua S. Sharp − *Department of Biomolecular Sciences and Department of Chemistry and Biochemistry, University of Mississippi, Oxford, Mississippi 38677, United States;* orcid.org/0000-0002-0115-0276; Email: jsharp@olemiss.edu

Authors

Ajay Sharma − *Department of Biomolecular Sciences, University of Mississippi, Oxford, Mississippi 38677, United States*

Suman Choudhary − *Department of Biomolecular Sciences, University of Mississippi, Oxford, Mississippi 38677, United States*

Sandeep K. Misra − *Department of Biomolecular Sciences, University of Mississippi, Oxford, Mississippi 38677, United States;* orcid.org/0000-0001-9165-3987

Anter A. Shami − *Department of Biomolecular Sciences, University of Mississippi, Oxford, Mississippi 38677, United States*

Sushil K. Mishra − *Department of Biomedical Engineering, University of Mississippi, Oxford, Mississippi 38677, United States;* orcid.org/0000-0002-3080-9754

Zachary C. Drake − *Department of Chemistry and Biochemistry, University of California, Los Angeles, California 90095, United States*

Steffen Lindert − *Department of Chemistry and Biochemistry, University of California, Los Angeles, California 90095, United States*

Complete contact information is available at: https://pubs.acs.org/10.1021/acs.analchem.5c06463

Notes

The authors declare the following competing financial interest(s): J.S.S. discloses a significant interest in GenNext Technologies, Inc., a growth-stage company seeking to commercialize technologies for protein higher-order structure analysis.

ACKNOWLEDGMENTS

The authors would also like to thank GenNext Technology for providing the Fox Photolysis System for this work. This work was supported by a grant from the National Institute of General Medical Sciences (R01GM127267). SEC-MALS analyses were supported by the Analytical and Biophysical Chemistry Core of the Glycoscience Center of Research Excellence, which is supported by an Institutional Development Award (IDeA) from the National Institute of General Medical Sciences of the National Institutes of Health under award number P20GM130460.

REFERENCES

(1) Petrotchenko, E. V.; Borchers, C. H. J. C. R. Protein chemistry combined with mass spectrometry for protein structure determination. *Chem. Rev.* **2022**, *122* (8), 7488−7499.

(2) Liang, F.; Sun, M.; Xie, L.; Zhao, X.; Liu, D.; Zhao, K.; Zhang, G. Recent advances and challenges in protein complex model accuracy estimation. *Comput. Struct. Biotechnol. J.* **2024**, *23*, 1824−1832.

(3) Wayment-Steele, H. K.; Ojoawo, A.; Otten, R.; Apitz, J. M.; Pitsawong, W.; Hömberger, M.; Ovchinnikov, S.; Colwell, L.; Kern, D. J. N. Predicting multiple conformations via sequence clustering and AlphaFold2. *Nature* **2024**, *625* (7996), 832−839.

(4) Kaur, P.; Kiselar, J.; Yang, S.; Chance, M. R. Quantitative protein topography analysis and high-resolution structure prediction using hydroxyl radical labeling and tandem-ion mass spectrometry (MS). *Mol. Cell. Proteomics* **2015**, *14* (4), 1159−1168.

(5) Xie, B.; Sood, A.; Woods, R. J.; Sharp, J. S. Quantitative Protein Topography Measurements by High Resolution Hydroxyl Radical Protein Footprinting Enable Accurate Molecular Model Selection. *Sci. Rep.* **2017**, *7* (1), 4552.

(6) Cornwell, O.; Ault, J. R. Fast photochemical oxidation of proteins coupled with mass spectrometry. *BBA-Proteins Proteomics* **2022**, *1870* (9), No. 140829.

(7) Jain, R.; Dhillon, N. S.; Kanchustambham, V. L.; Lodowski, D. T.; Farquhar, E. R.; Kiselar, J.; Chance, M. R. Evaluating Mass Spectrometry-Based Hydroxyl Radical Protein Footprinting of a Benchtop Flash Oxidation System against a Synchrotron X-ray Beamline. *J. Am. Soc. Mass Spectrom.* **2024**, *35* (3), 476−486.

(8) Sharp, J. S.; Chea, E. E.; Misra, S. K.; Orlando, R.; Popov, M.; Egan, R. W.; Holman, D.; Weinberger, S. R. Flash Oxidation (FOX) System: A Novel Laser-Free Fast Photochemical Oxidation Protein Footprinting Platform. *J. Am. Soc. Mass Spectrom.* **2021**, *32* (7), 1601−1609.

(9) Xu, G.; Chance, M. R. Radiolytic modification and reactivity of amino acid residues serving as structural probes for protein footprinting. *Anal. Chem.* **2005**, *77* (14), 4549−4555.

(10) Tadi, S.; Misra, S. K.; Sharp, J. S. Inline Liquid Chromatography-Fast Photochemical Oxidation of Proteins for Targeted Structural Analysis of Conformationally Heterogeneous Mixtures. *Anal. Chem.* **2021**, *93* (7), 3510−3516.

(11) Johnson, D. T.; Jones, L. M. Hydroxyl radical protein footprinting for analysis of higher order structure. *Trends Bioch. Sci.* **2022**, *47* (11), 989−991.

(12) Li, X.; Grant, O. C.; Ito, K.; Wallace, A.; Wang, S.; Zhao, P.; Wells, L.; Lu, S.; Woods, R. J.; Sharp, J. S. Structural Analysis of the Glycosylated Intact HIV-1 gp120-b12 Antibody Complex Using Hydroxyl Radical Protein Footprinting. *Biochemistry* **2017**, *56* (7), 957−970.

(13) Stocks, B. B.; Konermann, L. Structural characterization of short-lived protein unfolding intermediates by laser-induced oxidative labeling and mass spectrometry. *Anal. Chem.* **2009**, *81* (1), 20−27.

(14) McKenzie-Coe, A.; Montes, N. S.; Jones, L. M. Hydroxyl Radical Protein Footprinting: A Mass Spectrometry-Based Structural Method for Studying the Higher Order Structure of Proteins. *Chem. Rev.* **2022**, *122* (8), 7532−7561.

(15) Ralston, C. Y.; Sharp, J. S. Structural Investigation of Therapeutic Antibodies Using Hydroxyl Radical Protein Footprinting Methods. *Antibodies* **2022**, *11* (4), 71.

(16) Grandori, R. Protein structure and dynamics in the era of integrative structural biology. *Front. Biophys.* **2023**, *1*, 1219843.

(17) Puthenveetil, R.; Vinogradova, O. Solution NMR: A powerful tool for structural and functional studies of membrane proteins in

reconstituted environments. *J. Biol. Chem.* **2019**, *294* (44), 15914−15931.
(18) Cheng, Z.; Misra, S. K.; Shami, A.; Sharp, J. S. Structural Analysis of Phosphorylation Proteoforms in a Dynamic Heterogeneous System Using Flash Oxidation Coupled In-Line with Ion Exchange Chromatography. *Anal. Chem.* **2022**, *94* (51), 18017−18024.
(19) Aprahamian, M. L.; Chea, E. E.; Jones, L. M.; Lindert, S. Rosetta protein structure prediction from hydroxyl radical protein footprinting mass spectrometry data. *Anal. Chem.* **2018**, *90* (12), 7721−7729.
(20) Khaje, N. A.; Eletsky, A.; Biehn, S. E.; Mobley, C. K.; Rogals, M. J.; Kim, Y.; Mishra, S. K.; Doerksen, R. J.; Lindert, S.; Prestegard, J. H.; Sharp, J. S. Validated determination of NRG1 Ig-like domain structure by mass spectrometry coupled with computational modeling. *Commun. Biol.* **2022**, *5* (1), 452.
(21) Olson, S. T.; Srinivasan, K. R.; Björk, I.; Shore, J. D. Binding of high affinity heparin to antithrombin III. Stopped flow kinetic studies of the binding interaction. *J. Biol. Chem.* **1981**, *256* (21), 11073−11079.
(22) Noreika, V. A.; Wecksler, A. T. Footprinting for fingerprinting: proof-of-concept for the use of hydroxyl radical protein footprinting for structural comparison studies. *mAbs* **2025**, *17* (1), 2530575.
(23) Weinberger, S. R.; Chea, E. E.; Sharp, J. S.; Misra, S. K. Laser-free Hydroxyl Radical Protein Footprinting to Perform Higher Order Structural Analysis of Proteins. *J. Vis. Exp.* **2021**, (172).
(24) Xie, B.; Sharp, J. S. Hydroxyl Radical Dosimetry for High Flux Hydroxyl Radical Protein Footprinting Applications Using a Simple Optical Detection Method. *Anal. Chem.* **2015**, *87* (21), 10719−10723.
(25) Sharp, J. S.; Misra, S. K.; Persoff, J. J.; Egan, R. W.; Weinberger, S. R. Real Time Normalization of Fast Photochemical Oxidation of Proteins Experiments by Inline Adenine Radical Dosimetry. *Anal. Chem.* **2018**, *90* (21), 12625−12630.
(26) Cheng, Z.; Mobley, C.; Misra, S. K.; Gadepalli, R. S.; Hammond, R. I.; Brown, L. S.; Rimoldi, J. M.; Sharp, J. S. Self-Organized Amphiphiles Are Poor Hydroxyl Radical Scavengers in Fast Photochemical Oxidation of Proteins Experiments. *J. Am. Soc. Mass Spectrom.* **2021**, *32* (5), 1155−1161.
(27) Misra, S. K.; Orlando, R.; Weinberger, S. R.; Sharp, J. S. Compensated Hydroxyl Radical Protein Footprinting Measures Buffer and Excipient Effects on Conformation and Aggregation in an Adalimumab Biosimilar. *AAPS J.* **2019**, *21* (5), 87.
(28) Hambly, D. M.; Gross, M. L. Laser flash photolysis of hydrogen peroxide to oxidize protein solvent-accessible residues on the microsecond timescale. *J. Am. Soc. Mass Spectrom.* **2005**, *16* (12), 2057−2063.
(29) Saladino, J.; Liu, M.; Live, D.; Sharp, J. S. Aliphatic peptidyl hydroperoxides as a source of secondary oxidation in hydroxyl radical protein footprinting. *J. Am. Soc. Mass Spectrom.* **2009**, *20* (6), 1123−1126.
(30) Xu, G.; Chance, M. R. Hydroxyl radical-mediated modification of proteins as probes for structural proteomics. *Chem. Rev.* **2007**, *107* (8), 3514−3543.
(31) Perez-Riverol, Y.; Bandla, C.; Kundu, D. J.; Kamatchinathan, S.; Bai, J.; Hewapathirana, S.; John, N. S.; Prakash, A.; Walzer, M.; Wang, S.; Vizcaíno, J. A. The PRIDE database at 20 years: 2025 update. *Nucleic Acids Res.* **2025**, *53* (D1), D543−d553.
(32) Chen, J.; Rempel, D. L.; Gau, B. C.; Gross, M. L. Fast photochemical oxidation of proteins and mass spectrometry follow submillisecond protein folding at the amino-acid level. *J. Am. Soc. Mass Spectrom.* **2012**, *134* (45), 18724−18731.
(33) Gau, B. C.; Chen, J.; Gross, M. L. Fast photochemical oxidation of proteins for comparing solvent-accessibility changes accompanying protein folding: data processing and application to barstar. *Biochim. Biophys. Acta* **2013**, *1834* (6), 1230−1238.
(34) Clerc, F.; Reiding, K. R.; Jansen, B. C.; Kammeijer, G. S.; Bondt, A.; Wuhrer, M. Human plasma protein N-glycosylation. *Glycoconj. J.* **2016**, *33* (3), 309−343.
(35) Abramson, J.; et al. Accurate structure prediction of biomolecular interactions with AlphaFold 3. *Nature* **2024**, *630* (8016), 493−500.
(36) Lee, J.; Cheng, X.; Jo, S.; MacKerell, A. D.; Klauda, J. B.; Im, W. 534 Charmm-gui input generator for namd, gromacs, amber, openmm, and charmm/openmm simulations 535 using the charmm36 additive force field. *Biophys. J.* **2016**, *110* (3), 641a.
(37) Park, S. J.; Lee, J.; Qi, Y.; Kern, N. R.; Lee, H. S.; Jo, S.; Joung, I.; Joo, K.; Lee, J.; Im, W. CHARMM-GUI Glycan Modeler for modeling and simulation of carbohydrates and glycoconjugates. *Glycobiology* **2019**, *29* (4), 320−331.
(38) Huang, J.; MacKerell, A. D., Jr CHARMM36 all-atom additive protein force field: Validation based on comparison to NMR data. *J. Comput. Chem.* **2013**, *34* (25), 2135−2145.
(39) Jorgensen, W. L.; Chandrasekhar, J.; Madura, J. D.; Impey, R. W.; Klein, M. L. Comparison of simple potential functions for simulating liquid water. *J. Chem. Phys.* **1983**, *79* (2), 926−935.
(40) Ryckaert, J. P.; Ciccotti, G.; Berendsen, H. J. C. Numerical integration of the cartesian equations of motion of a system with constraints: molecular dynamics of n-alkanes. *J. Comput. Phys.* **1977**, *23* (3), 327−341.
(41) Brooks, B. R.; et al. CHARMM: the biomolecular simulation program. *J. Comput. Chem.* **2009**, *30* (10), 1545−1614.
(42) Phillips, J. C.; et al. Scalable molecular dynamics on CPU and GPU architectures with NAMD. *J. Chem. Phys.* **2020**, *153* (4), No. 044130.
(43) Pletcher, C. H.; Cunningham, M. T.; Nelsestuen, G. L. Molecular weight analysis of antithrombin III-heparin and antithrombin III-thrombin-heparin complexes. *J. Biol. Chem.* **1986**, *261* (9), 4143−4147.
(44) Rashid, Q.; Abid, M.; Jairajpuri, M. A. Elucidating the specificity of non-heparin-based conformational activators of antithrombin for factor Xa inhibition. *J. Nat. Sci. Biol. Med.* **2014**, *5* (1), 36−42.
(45) Richard, B.; Swanson, R.; Izaguirre, G.; Olson, S. T. Cooperative Interactions of Three Hotspot Heparin Binding Residues Are Critical for Allosteric Activation of Antithrombin by Heparin. *Biochemistry* **2018**, *57* (15), 2211−2226.
(46) Ersdal-Badju, E.; Lu, A.; Zuo, Y.; Picard, V.; Bock, S. C. Identification of the antithrombin III heparin binding site. *J. Biol. Chem.* **1997**, *272* (31), 19393−19400.
(47) Jin, L.; Abrahams, J. P.; Skinner, R.; Petitou, M.; Pike, R. N.; Carrell, R. W. The anticoagulant activation of antithrombin by heparin. *PNAS USA* **1997**, *94* (26), 14683−14688.
(48) Skinner, R.; Abrahams, J. P.; Whisstock, J. C.; Lesk, A. M.; Carrell, R. W.; Wardell, M. R. The 2.6 A structure of antithrombin indicates a conformational change at the heparin binding site. *J. Mol. Biol.* **1997**, *266* (3), 601−609.
(49) Schedin-Weiss, S.; Desai, U. R.; Bock, S. C.; Gettins, P. G.; Olson, S. T.; Björk, I. Importance of lysine 125 for heparin binding and activation of antithrombin. *Biochemistry* **2002**, *41* (15), 4779−4788.
(50) Listigovers, A.; Lento, C.; Wilson, D. J. Distinct antithrombin activation modes for fondaparinux and natural heparins detected using millisecond hydrogen deuterium exchange and collision induced unfolding. *Int. J. Biol. Macromol.* **2024**, *273* (Pt 1), No. 132868.
(51) McCoy, A. J.; Pei, X. Y.; Skinner, R.; Abrahams, J. P.; Carrell, R. W. Structure of beta-antithrombin and the effect of glycosylation on antithrombin's heparin affinity and activity. *J. Mol. Biol.* **2003**, *326* (3), 823−833.

https://doi.org/10.1021/acs.analchem.5c06463
Anal. Chem. 2026, 98, 6045−6055